Nat. Hazards Earth Syst. Sci. Discuss., 3, 1949–1970, 2015
www.nat-hazards-earth-syst-sci-discuss.net/3/1949/2015/
doi:10.5194/nhessd-3-1949-2015


Natural Hazards and Earth System Sciences
Open Access
Discussions



# Source of the 6 February 2013 $M_w$ 8.0 Santa Cruz Islands Tsunami

**F. Romano, I. Molinari, S. Lorito, and A. Piatanesi**

Istituto Nazionale di Geofisica e Vulcanologia, Via di Vigna Murata 605, 00143, Rome, Italy

Received: 27 February 2015 – Accepted: 3 March 2015 – Published: 16 March 2015

Correspondence to: F. Romano (fabrizio.romano@ingv.it)

Published by Copernicus Publications on behalf of the European Geosciences Union.







## Abstract

On 6 February 2013 an $M_w$ 8.0 subduction earthquake occurred close to Santa Cruz Islands at the transition between the Solomon and the New Hebrides Trench. The ensuing tsunami caused significant inundation on the closest Nendo Island. The seismic source was studied with teleseismic broadband P waves inversion optimized with tsunami forward modeling at DART buoys (Lay et al., 2013), and with inversion of teleseismic body and surface waves (Hayes et al., 2014). The two studies also use different hypocenters and different planar fault models, and found quite different slip models. In particular, Hayes et al. (2014) argued for an aseismic slip patch SE from the hypocenter. We here develop a 3-D model of the fault surface from seismicity analysis and retrieve the tsunami source by inverting DART and tide-gauge data. Our tsunami source model features a main slip patch (peak value of ∼ 11 m) SE of the hypocentre, and reaching to the trench. The rake direction is consistent with the progressively more oblique plate convergence towards the Solomon trench. The tsunami source partially overlaps the hypothesized aseismic slip area, which then might have slipped coseismically.

## 1 Introduction

On 6 February 2013 an $M_w$ 8.0 earthquake occurred in the Pacific Ocean nearby the archipelago of Santa Cruz Islands. The hypocenter (165.138° E 10.738° S, depth ∼ 29 km, USGS, http://comcat.cr.usgs.gov/earthquakes/eventpage/usc000f1s0#summary) is located at the subduction interface between the Australia and the Pacific plates, 76 km West from Lata, the main city of Nendo Island (Figs. 1 and 2).

This earthquake, the largest in 2013, occurred on a complex section of the Australia-Pacific plate boundary at the northern end of the New Hebrides trench (Hayes et al., 2012), nearby a short segment of dominantly strike-slip plate motion that marks the transition between Vanuatu and the Solomon Islands subduction zones. This seg-





NHESSD
3, 1949–1970, 2015



ment is characterized by a complex tectonic regime that becomes progressively more oblique westward as revealed by the focal mechanisms of the local seismicity (Fig. 1). In this region the relative convergence velocity between Australia and Pacific plates is $\sim 9.4\,\mathrm{cm\,yr^{-1}}$ (DeMets et al., 2010).

The Santa Cruz Islands earthquake generated a tsunami that struck the Nendo Island, in particular the city of Lata with waves higher than 1 m. Several runup and flowdepth measurements have been collected during a field survey conducted on some islands of the archipelago few days after the earthquake (Fritz et al., 2014), reporting maximum tsunami wave heights of about 11 m in the western part of the Nendo Island. In addition, the tsunami propagated in the Pacific Ocean, also reaching the coasts of Hawaii (Lay et al., 2013).

Seismic and tsunami source of this earthquake have been previously studied with different methodologies (Lay et al., 2013; Hayes et al., 2014a), highlighting some differences between the resulting models in terms of both slip patches position and slip amplitude. Hayes et al. (2014a) studied the Santa Cruz Islands earthquake by inverting teleseismic body and surface waves; Lay et al. (2013) performed a teleseismic broadband P waves inversion optimized with tsunami forward modelling at DART buoys. These studies used different hypocenters and different planar fault models; in particular, Lay et al. (2013) adopted both hypocenter and fault plane shallower than those used by Hayes et al. (2014a). The best-fitting source model in Hayes et al. (2014a, hereinafter HA14) has a main patch of slip centred around the hypocenter with a maximum slip of about 4 m and a second smaller patch located SE of the Nendo Island and characterized by relatively low slip ($\sim 0.5$ m). On the other hand, the source model in Lay et al. (2013, hereinafter LA13) features two patches with slip larger than 10 m; the first patch is located around the hypocenter, whereas the second one is shallower and located SE of the hypocenter. The surface projection of the slip in LA13 is roughly consistent with the HA14 patches even if they are at different depths (and featuring quite different slip values), because of the different fault planes used. In addition, the





NHESSD
3, 1949–1970, 2015



LA13 source model is more efficient in terms of tsunami waves excitation than that of HA14 and quite well predicts the tsunami observations recorded at the DART buoys.

The usual pattern of the aftershocks distribution following a great subduction earthquake should show a large number of events occurring at the subduction interface not dislocated, eventually also bordering the broken asperities (Aki, 1979). On the other hand, as already extensively discussed (Hayes et al., 2014a; Lay et al., 2013), after the 2013 6 February event, very few events were located along the subduction interface. Furthermore, most of early aftershocks in the epicentral area (~ 200 events within 48 h from the mainshock, USGS catalogue, http://earthquake.usgs.gov/earthquakes/) showed strike-slip and normal mechanism, including two earthquakes with $M_w > 7$ occurred in the upper crust portion of the Pacific plate and in the outer-rise trench region. Hayes et al. (2014a) proposed a block-like motion behaviour of the Pacific upper plate to explain these observations. In particular, they argued that a large number of anomalous right-lateral strike-slip events located southeast of Nendo Island were triggered by significant aseismic slip along a portion of the megathrust south-eastward from the epicentral area. However, LA13 model features significant coseismic slip on this portion of the fault; these differences may be due to the different data used and/or to the different fault models adopted in the inversions.

Here we study the coseismic tsunami source of the Santa Cruz Islands earthquake by inverting the available tsunami waveforms. We compute the Green's functions at the DART buoys and tide gauges using a 3-D fault model that honours the complex geometry of the subduction interface. After retrieving the tsunami source model, we discuss it in comparison with LA13 and HA14 source models.

## 2 Tsunami data and fault model

The tsunami generated by the Santa Cruz Islands earthquake propagated both in the North and South Pacific Ocean and it has been observed in the open sea at several DART buoys and at some tide gauges located along the coasts of Solomon and





NHESSD
3, 1949–1970, 2015



Fiji Islands. We select 5 DART buoys (52 403, 52 406, 51 425, 55 012, and 55 023, http://www.ndbc.noaa.gov/dart.shtml) and 3 tide gauges (Lata Wharf, Honiara, and Lautoka, http://www.ioc-sealevelmonitoring.org) that distinctly recorded a tsunami signal and that allows a good azimuthal coverage (Fig. 2, further details in Supplement). Before using the tsunami data in the inversion, we remove the tide from the original signals by using a robust LOWESS procedure (Barbosa et al., 2004).

The fault model geometry can greatly influence the results of source inversion. Adopting a fault geometry that honours the complexities of the subduction interface then may help to reduce the epistemic uncertainties associated to forward modelling (Romano et al., 2014). This is particularly true for earthquakes of this size occurring in subduction zones characterized by strong variations of strike and/or dip (e.g. Hayes et al., 2014b), even more so in complex tectonic environments like the Santa Cruz Islands region.

Thus, analysing the aftershocks distribution occurred after the 6 February mainshock, the local seismicity, and considering the rupture area expected for a M8 event, we built a 3-D non-planar fault model with variable strike and dip angles in order to account for such geometrical complexities of the subduction interface on both the New Hebrides and Solomon trenches (Bird, 2003). In particular, we selected from the EHB global relocation earthquake catalogue (http://www.isc.ac.uk/ehbbulletin/; Engdahl et al., 1998) the events occurred in the area covered by the aftershocks of the Santa Cruz Islands earthquake and having $M > 4.5$. After removing those ones relatively distant from the trench (distance > 200 km), we drew sections perpendicular to the trench at a distance of ~ 20 km each (measured along the trench) and we projected on them all the events in a neighbourhood of 30 km. We obtained several 2-D profiles by fitting the data of each section. The resulting suite of 2-D profiles was then further interpolated using CUBIT software (http://cubit.sandia.gov) in order to obtain a 3-D fault model, meshed into 45 quadrangular patches (9 along strike and 5 along dip, Figs. 2, S1 and S2) with an average size of about 20 km × 20 km. Our final fault model is consistent with the northern interface of Vanuatu slab model in Slab1.0 (Hayes et al.,





NHESSD
3, 1949–1970, 2015



2012, http://earthquake.usgs.gov/data/slab/) and extends both up to the trench and in the north-west direction for ∼ 40–60 km. The dimensions of the resulting fault are ∼ 180 km along strike and ∼ 90 km along dip (see Figs. 2, S1 and S2).

## 3 Green's functions and inversion scheme

The tsunami Green's functions are computed by means of NEOWAVE, a nonlinear dispersive model for tsunami waves propagation (Yamazaki et al., 2009, 2011). The initial conditions for tsunami propagation are analytically computed (further details in Meade, 2007; Romano et al., 2012) and they also include the contribution of the coseismic horizontal deformation in the region of steep bathymetric slopes (Tanioka and Satake, 1996).

For tsunami modelling at the DART buoys we use a bathymetric grid with a spatial resolution of 1 arc-min, whereas the Green's functions at the tide gauges are computed on a grid of 30 arc-sec in order to better model the nearshore tsunami propagation. The bathymetric data set used for tsunami simulations is SRTM30+ (http://topex.ucsd.edu/WWW_html/srtm30_plus.html), which is resampled for the grid of 1 arc-min.

We solve the inverse problem by using the Heat Bath algorithm, which is a particular implementation of the Simulated Annealing technique (Rothman, 1986). For tsunami waveforms we use a cost function that is sensitive both to amplitude and phase matching (Spudich and Miller, 1990). This approach and the a-posteriori analysis of the explored ensemble of models have been extensively tested and used in previous works (detailed description of the method can be found for example in Piatanesi and Lorito, 2007; Lorito et al., 2011; Romano et al., 2014, and references therein).

We make some a-priori assumptions on ranges for slip and rake: for each subfault the slip can vary from 0 to 15 m at 0.5 m steps, whereas the rake can vary from 40 to 100° at 5° steps on 3 large blocks (see Fig. S1). Furthermore, we assume a circular rupture front that propagates with a rupture velocity of 1.5 km s$^{-1}$ (Lay et al., 2013).





NHESSD
3, 1949–1970, 2015



In each inversion we retrieve the best fitting slip distribution model, the average model obtained by the ensemble of models that fits the data fairly well, and the SDs for each inferred model parameter (e.g. Table S3).

### 3.1 Checkerboard resolution test

We evaluate the resolving power of the inversion setup (i.e., fault parameterization and instrumental azimuthal coverage) by means of a synthetic test. In particular, we attempt to reproduce a slip distribution assuming a target checkerboard pattern with slip values of 0 and 10 m on alternating subfaults (Fig. 3a). In addition, we set the target rake angle on the easternmost, middle, and westernmost blocks equal to 90, 70, and 50°, respectively. We invert the synthetic tsunami waveforms resulting from the target slip pattern by following the same inversion procedure described above. The average model for slip distribution (Fig. 3b) reproduces very well the checkerboard target (Fig. 3a). We observe that the maximum differences between the target and the retrieved slip models are smaller than 1 m (absolute value). The chosen inversion setup is also well calibrated to recover the target slip direction (i.e., the rake angle) on the fault plane, and the comparison between the synthetic and predicted tsunami waveforms shows an excellent agreement (Fig. S3).

## 4 Source of the 2013 Santa Cruz Islands tsunami

We use the same inversion scheme, fault parameterization, and set of DART buoys and tide gauges data used for the checkerboard test to retrieve the coseismic tsunami source of the Santa Cruz Islands earthquake. The coseismic rupture pattern (average model, Table S3) shows a main patch of slip (Fig. 4), located SE from the hypocenter, centred around ~ 165.5° E ~ 11° S, and featuring a maximum slip value of ~ 11 m at a depth of ~ 25 km. The coseismic rupture reaches the shallowest portion of the subduction interface and it spreads along strike in NW direction with maximum slip values





NHESSD
3, 1949–1970, 2015



of ∼ 6 m. The dislocation model resulting from the inversion shows a second smaller patch of slip located NW from the hypocenter and centred at a depth of ∼ 29 km around ∼ 165° E ∼ 10.5° S (Fig. 4). This patch has a maximum slip of ∼ 4 m. We found an average rake angle of ∼ 85° in the easternmost part of the fault that is consistent with the relative convergence of the Australia and Pacific plates in this portion of the megathrust. On the other hand, the remaining part of the fault plane to the west is characterized by a slip angle lower than 50°. Hence, the dislocation there highlights a relevant strike-slip component, according with the change of the tectonic regime in this region, from purely thrust to left-lateral, as also shown by the regional seismicity. Figure 5 shows an overall good agreement between observed and predicted tsunami waveforms. During the inversion we applied a time shift (+2 min) to the Green's functions of Lata Wharf tide gauge due to the systematic anticipation of the predicted tsunami waveform with respect to the observed signal. This systematic difference between observed and predicted data is likely due to the relatively low accuracy of the nearshore bathymetry around this station. The total seismic moment associated to the slip distribution resulting from the inversion, using a shear modulus equal to 30 GPa, is $M_0 = 1.033 \times 10^{21}$ Nm, that is equivalent to a moment magnitude $M_w = 8.0$ and in agreement with the estimations obtained from previous studies.

## 5 Discussion

In principle, teleseismic data well constrain the earthquake seismic moment and the seismic rupture history, and, compared to tsunami data, they are less sensitive to the spatial details of the slip distribution (e.g. Yue, 2014). Moreover, adopting different fault geometries may result in different earthquake slip distributions. The possibility of trade-off between the hypocentral depth, or the fault model, assumed during the inversion and both the resulting location and amount of slip is well known (e.g. Baba et al., 2009), with evident effects on the associated tsunami waves excitation.





NHESSD
3, 1949–1970, 2015



The comparison among the present model, LA13, and HA14 shows some differences in terms of tsunami source that may be ascribed to the different data and fault model used in the inversions.

The slip model in this study, LA13, and HA14 models have been obtained using three different fault geometries (Fig. 6). Indeed, both LA13 and HA14 use a planar fault, whereas we adopt a 3-D fault surface honouring the subduction zone interface. In addition, the fault in LA13 is overall shallower with respect to that in HA14, and LA13 also assumes a shallower hypocenter ($\sim$ 13 km, whereas it is $\sim$ 29 km in HA14, compare Fig. 6b and d).

As shown in Lay et al. (2013), the slip distributions of the Santa Cruz Islands earthquake obtained by using only teleseismic data, adopting a hypocenter deeper than 15 km, and an overall deeper fault plane result in an under-prediction of tsunami observations at DART buoys. For this reason, Lay et al. (2013) prefer, among teleseismic solutions, the one obtained by imposing a shallower hypocenter. Since the model in this study and LA13 explain tsunami data to a similar extent, then the main differences between the two may be ascribed either to differences in the adopted fault geometry, or to poor resolving power of tsunami data themselves, which would lead to non uniqueness of the solution. According to our synthetic test, the latter does not seem to be the case, at least as regards the most tsunamigenic part of the source, that is the one with a dominant dip slip component in LA13 model. Besides this, we also may argue that the HA14 source, which shows a deeper slip centroid than LA13 (and lower peak slip of about 4 m, Fig. 6a), should result less tsunamigenic with respect to LA13 (peak slip > 10 m, Fig. 6c), and then likely underestimate tsunami observations.

The centroid of the main asperity individuated in the present study is shifted SE with respect to the main one of HA14 and it features quite larger slip (Fig. 6a). Conversely, it features comparable peak slip values to the shallower patch in LA13 (Fig. 6c), but it is nearer to the Nendo Island, as the two are only partially overlapped.

We also observe that the rake angle associated to our model is pretty consistent with the relative convergence direction between Australia and Pacific plates. In partic-





NHESSD
3, 1949–1970, 2015



ular, the slip direction has behaviour close to a thrust-like motion (rake ∼ 85°) in the SE part of the fault just nearby the northern-end of Vanuatu subduction zone; then the slip direction becomes progressively more oblique highlighting a significant left-lateral component that is in agreement with the kinematics (DeMets et al., 2010) and the seismicity of the NW segment of the subduction (Fig. 1). On the other hand, we observe an opposite behaviour of the rake angle in LA13; indeed, the southeastern shallower patch in LA13 has a slip direction with a strong oblique component, whereas the northern deeper patch shows a thrust-like fault motion. Thus, the main tsunamigenic patch in LA13 is located around the hypocenter, whereas in the present study it is located in front of the Nendo Island, very close to the area where the maximum tsunami wave heights have been observed (Fig. 1; Fritz et al., 2014; NOAA/NGDC, http://www.ngdc.noaa.gov/hazard/tsu_db.shtml). Hence, as a likely less tsunamigenic patch is involved, these differences may be due to a combination of the effects of different resolving power of the data used and of different fault geometry.

In a further analysis, we compare the rupture front that we imposed in the inversion with the resulting slip distribution; we observe that ∼ 97 % of the total seismic moment has been released within 75 s from the nucleation. In particular, ∼ 60 % of the moment release occurred between 15 and 45 s, a time window including most of the main asperity and the peak slip area (Fig. 4). Thus, despite of the differences among the models, and even though tsunami data are not particularly suitable to resolve the details of the seismic rupture history, our source model, at least at the first order, is in agreement with the moment rate functions resulting from studies that used teleseismic data.

The distribution of the early aftershocks (in the first 48 h after the mainshock, USGS catalogue, http://earthquake.usgs.gov/earthquakes/), shows a lack of significant seismic events occurring at the subduction interface, a feature that might be indicative of a complete stress drop associated to the main 6 February event. On the other hand, a large number of seismic events have been observed mainly in the upper crust of the Pacific plate and in the eastern edge of the Australia plate oceanic crust (Fig. 4). In particular, the largest one in the Pacific plate ($M_w$7+) occurred North of Nendo Island





NHESSD
3, 1949–1970, 2015



with a strike-slip right-lateral mechanism (Fig. 1) that is consistent with the kinematics of the coseismic slip (Hayes et al., 2014a). In addition, a cluster of shallow right-lateral aftershocks occurred SE from the mainshock epicenter (magenta ellipse in Fig. 4). In their study, Hayes et al. (2014a) propose that occurrence of these strike-slip earthquakes is caused by the block-like motion behaviour of the Pacific upper plate. However, they also argue that the Coulomb stress change distribution resulting from the HA14 coseismic model would promote events with left-lateral behaviour, whereas significant additional slip located SE from the hypocenter would promote the observed right-lateral aftershocks. They conclude that such slip (see magenta shaded ellipse in Fig. 6a), as not observed in HA14, then should be aseismic, should occur at the megathrust interface, and, in agreement with the Coulomb stress transfer estimation, should release a seismic moment of $M_0 = 3.1 \times 10^{20}$ Nm. Thus, the total (coseismic + aseismic) seismic moment released along the southeastern portion of the fault results to be $M_0 = 3.9 \times 10^{20}$ Nm. Noteworthy, our slip model is partially overlapped with the aseismic slip area argued by Hayes et al. (2014a); in particular, we observe larger slip values, up to 9 m confined in a smaller area, vs. an average of 2 m of slip on a larger portion of the megathrust (Fig. 6a). The seismic moment associated to this portion of slip distribution in our model is $M_0 = 4.08 \times 10^{20}$ Nm, that is quite compatible with the estimation by Hayes et al. (2014a).

The location of the coseismic tsunami source that we found here is not in contradiction with the images of the rupture propagation resulting from back-projection analyses (IRIS, http://ds.iris.edu/spud/backprojection/1065729). Indeed, all of these analyses, while showing different features depending on the seismic network employed, highlight a possible rupture propagation south-eastward from the hypocenter, shown as well by the slip models obtained using tsunami data (this study and LA13). Furthermore, on one hand in the back-projection analyses the surface projection of the radiated energy shows coherent high-frequency radiation along a portion of the megathrust corresponding to the seismogenic layer; on the other hand, the coherence of seismic high-frequency radiation appears to degrade south-eastward at shallower depths. This





NHESSD
3, 1949–1970, 2015



feature, along with the slip propagation up to the trench (a zone likely rich of sediments) and the relatively low rupture velocity (1.5 km s$^{-1}$, Lay et al., 2013) suggests that part of the seismic rupture SE of Nendo Island may have been characterized by slow slip, as indicated by Lay et al. (2013). Therefore, we cannot rule out that this portion of the megathrust, at least partially, may have slipped coseismically triggering the right-lateral strike-slip aftershocks.

## 6 Conclusions

We retrieved the coseismic tsunami source of the 2013 Santa Cruz Islands earthquake by inverting tsunami observations recorded in the Pacific Ocean by several DART buoys and tide gauges. We also computed the Green's functions using a 3-D fault model honouring the geometrical complexities of the subduction interface. The retrieved coseismic tsunami source is mainly located SE from the hypocenter, with maximum slip value of ∼ 11 m and with the coseismic rupture reaching the shallow part of the megathrust with slip amplitudes up to 6 m. The seismic moment resulting from our coseismic slip model is equivalent to an $M_w$ 8.0 moment magnitude, in agreement with previous studies. The spatial pattern of the tsunami source is in agreement with the Australia and Pacific plates convergence direction that becomes progressively more oblique in the NW segment, and the slip distribution well reproduces the tsunami data. However, our model, compared with previously published models, features some differences in terms of tsunamigenesis and pattern of coseismic slip, that we have discussed in relation to the different resolving power of the data used and on the different fault geometry adopted. A common feature to all the models is the presence of slip SE from the hypocentre, which we argue to have occurred during the coseismic stage, possibly with a slow slip component, rather than being aseismic as previously suggested.





NHESSD
3, 1949–1970, 2015



**The Supplement related to this article is available online at doi:10.5194/nhessd-3-1949-2015-supplement.**

*Author contributions.* F. Romano was involved in all of the phases of this study. I. Molinari built the 3-D fault geometry, processed tsunami data, and contributed to write the paper. S. Lorito and A. Piatanesi contributed to design the experiment, to discuss and interpret the results and writing the paper. All authors reviewed the final manuscript.

*Acknowledgements.* This work is partially funded by project ASTARTE – Assessment, Strategy And Risk Reduction for Tsunamis in Europe – FP7-ENV2013 6.4-3, Grant 603839, and by the Italian flagship project RITMARE. Some of the figures in this work were drawn using GMT software (Wessel and Smith, 1995) and Matlab (http://www.mathworks.it/products/matlab/).

## References

Aki, K.: Characterization of barriers on an earthquake fault, J. Geophys. Res., 84, 6140–6148, 1979.

Baba, T., Cummins, P. R., Thio, H. K., and Tsushima, H.: Validation and joint inverison of teleseismic waveforms for earthquake source models using deep ocean bottom pressure records: a case study of the 2006 Kuril megathrust earthquake, Pure Appl. Geophys., 166, 55–76, doi:10.1007/s00024-008-0438-1, 2009.

Barbosa, S. M., Fernandes, M. J., and Silva, M. E.: Nonlinear sea level trends from European tide gauge records, Ann. Geophys., 22, 1465–1472, doi:10.5194/angeo-22-1465-2004, 2004.

Bird, P.: An updated digital model of plate boundaries, Geochem. Geophys. Geosyst., 4, 1027, doi:10.1029/2001GC000252, 2003.

DeMets, C., Gordon, R. G., and Argus, D. F.: Geologically current plate motions, Geophys. J. Int., 181, 1–80, doi:10.1111/j.1365-246X.2009.04491.x, 2010.

Engdahl, E. R., van der Hilst, R., and Buland, R.: Global teleseismic earthquake relocation with improved travel times and procedures for depth determination, B. Seismol. Soc. Am., 88, 722–743, 1998.





NHESSD

3, 1949–1970, 2015



Fritz, H. M., Papantoniou, A., Biukoto, L., Gilly, A., and Wei, Y.: The Solomon Islands Tsunami of 6 February 2013 in the Santa Cruz Islands: field Survey and Modeling, EGU General Assembly 2014, 27 April–2 May, Vienna, Austria, id.15777, 2014.

Hayes, G. P., Wald, D. J., and Johnson, R. L.: Slab1.0: a three-dimensional model of global subduction zone geometries, J. Geophys. Res., 117, B01302, doi:10.1029/2011JB008524, 2012.

Hayes, G. P., Furlong, K. P., Benz, H. M., and Herman, H. W.: Triggered aseismic slip adjacent to the 6 February 2013 $M_w$ 8.0 Santa Cruz Islands megathrust earthquake, Earth Planet. Sci. Lett., 388, 265–272, doi:10.1016/j.epsl.2013.11.010, 2014a.

Hayes, G. P., Herman, M. W., Banhart, W. D., Furlong, K. P., Riquelme, S., Benz, H. M., Bergman, E., Barrientos, S., Earle, P. S., and Samsonov, S.: Continuing megathrust earthquake potential in Chile after the 2014 Iquique earthquake, Nature, 512, 295–298, doi:10.1038/nature13677, 2014b.

Lay, T., Ye, L., Kanamori, H., Yamazaki, Y., Cheung, K. F., and Ammon, C. J.: The 6 February 2013 $M_w$ 8.0 Santa Cruz Islands earthquake and tsunami, Tectonophysics, 608, 1109–1121, doi:10.1016/j.tecto.2013.07.001, 2013.

Lorito, S., Romano, F., Atzori, S., Tong, X., Avallone, A., McCloskey, J., Cocco, M., Boschi, E., and Piatanesi, A.: Limited overlap between the seismic gap and coseismic slip of the great 2010 Chile earthquake, Nat. Geosci., 4, 173–177, doi:10.1038/NGEO1073, 2011.

Meade, B. J.: Algorithms for the calculation of exact displacements, strains, and stresses for triangular dislocation elements in a uniform elastic half space, Comput. Geosci., 33, 1064–1075, doi:10.1016/j.cageo.2006.12.003, 2007.

Piatanesi, A. and Lorito, S.: Rupture process of the 2004 Sumatra-Andaman earthquake from tsunami waveform inversion, B. Seismol. Soc. Am., 97, 223–231, doi:10.1785/0120050627, 2007.

Romano, F., Piatanesi, A., Lorito, S., D'Agostino, N., Hirata, K., Atzori, S., Yamazaki, Y., and Cocco, M.: Clues from joint inversion of tsunami and geodetic data of the 2011 Tohoku-oki earthquake, Sci. Rep., 2, 385, doi:10.1038/srep00385, 2012.

Romano, F., Trasatti, E., Lorito, S., Piromallo, C., Piatanesi, A., Ito, Y., Zhao, D., Hirata, K., Lanucara, P., and Cocco, M.: Structural control on the Tohoku earthquake rupture process investigated by 3-D FEM, tsunami and geodetic data, Sci. Rep., 4, 5631, doi:10.1038/srep05631, 2014.





NHESSD
3, 1949–1970, 2015



Rothman, D.: Automatic estimation of large residual statics corrections, Geophysics, 51, 332–346, doi:10.1190/1.1442092, 1986.

Spudich, P. and Miller, D. P.: Seismic site effects and the spatial interpolation of earthquake seismograms: results using aftershocks of the 1986 North Palm Springs, California, earthquake, B. Seismol. Soc. Am., 80, 1504–1532, 1990.

Tanioka, Y. and Satake, K.: Tsunami generation by horizontal displacement of ocean bottom, Geophys. Res. Lett., 23, 861–864, doi:10.1029/96GL00736, 1996.

Wessel, P. and Smith, W. H. F.: New version of the Generic Mapping Tools released, Eos Trans. AGU, 76, 329, doi:10.1029/95EO00198, 1995.

Yamazaki, Y., Kowalik, Z., and Cheung, K. F.: Depth-integrated, non-hydrostatic model for wave breaking, Int. J. Numer. Meth. Fl., 61, 473–497, doi:10.1002/fld.1952, 2009.

Yamazaki, Y., Cheung, K. F., and Kowalik, Z.: Depth-integrated, non-hydrostatic model with grid nesting for tsunami generation, propagation, and run-up, Int. J. Numer. Meth. Fl., 67, 2081–2107, doi:10.1002/fld.2485, 2011.

Yue, H.: Toward resolving stable high-resolution kinematic rupture models of large earthquakes by joint inversion of seismic, geodetic and tsunami observations, PhD Thesis, University of California, Santa Cruz, USA, 352 pp., available at: https://escholarship.org/uc/item/16j4870n, 2014.





NHESSD

3, 1949–1970, 2015



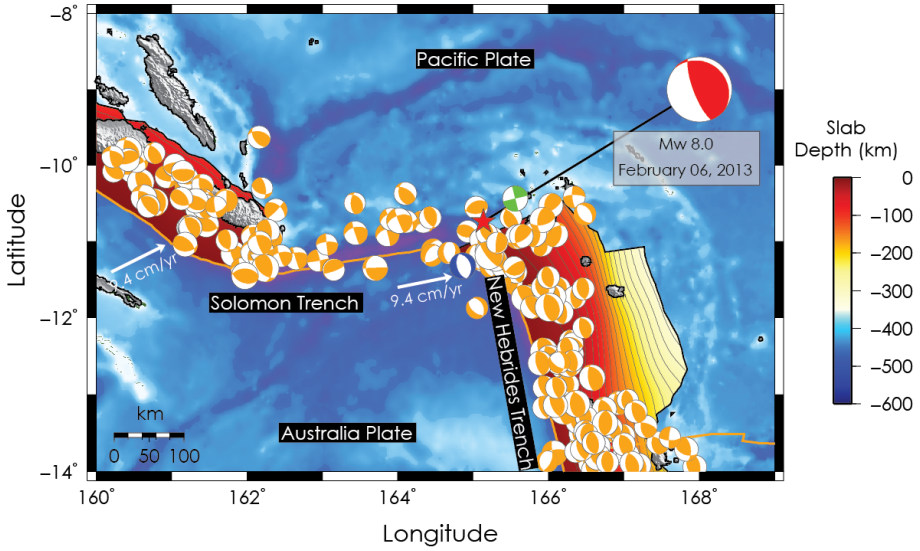


**Figure 1.** Location map of the 2013 Santa Cruz Islands earthquake. Red star and red beach ball indicate epicenter and focal mechanism of the mainshock, respectively. Green and blue beach balls indicate the focal mechanisms of the largest strike-slip ($M_w$ 7.0) and normal ($M_w$ 7.1) aftershocks occurred few hours after the mainshock. Orange beach balls indicate the regional historical seismicity (since 1976 to present, GCMT catalogue, http://www.globalcmt.org/CMTsearch.html) and the corresponding focal mechanisms for earthquake magnitude 6+. White arrows indicate the convergence direction of the Australia Plate.





NHESSD
3, 1949–1970, 2015



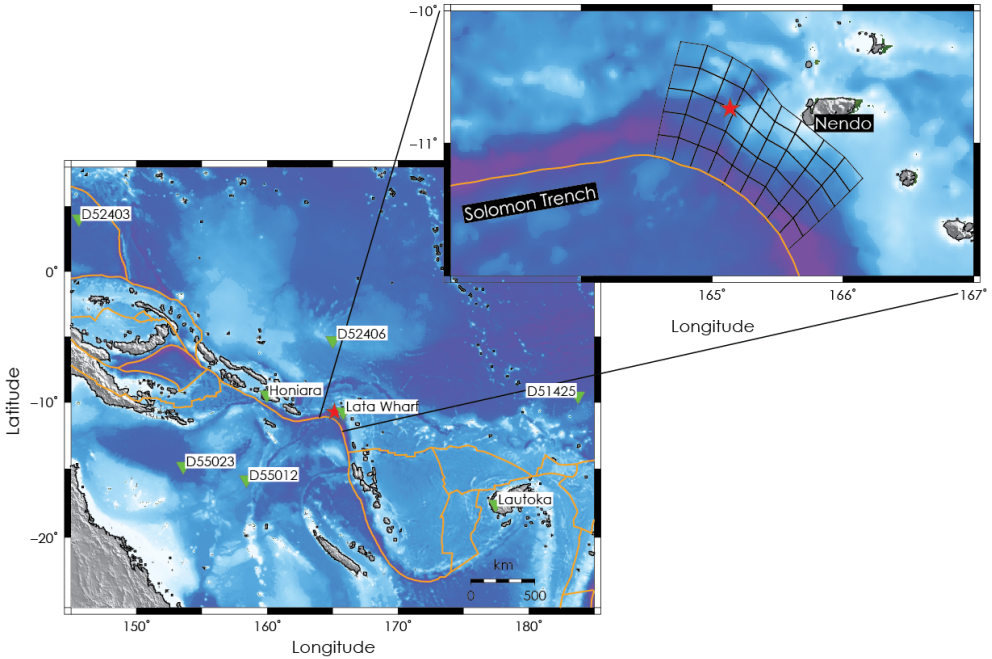


**Figure 2.** Data and fault model. Green triangles indicate DART buoys and tide gauges used in this study. The top-right panel is a close-up view of the fault model adopted. Red star indicates the Santa Cruz Islands earthquake epicenter.





NHESSD
3, 1949–1970, 2015



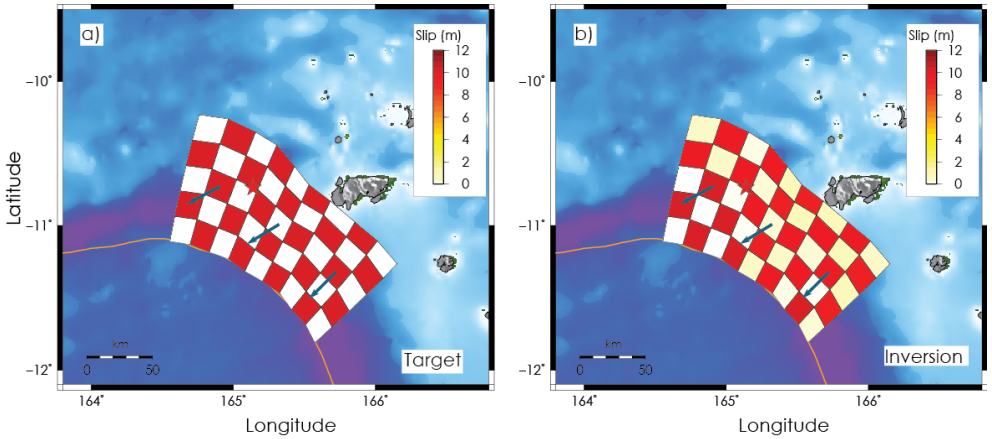


**Figure 3.** Resolution test. **(a)** Target slip and rake (blue arrows) pattern; **(b)** slip model obtained inverting tsunami data.





NHESSD
3, 1949–1970, 2015



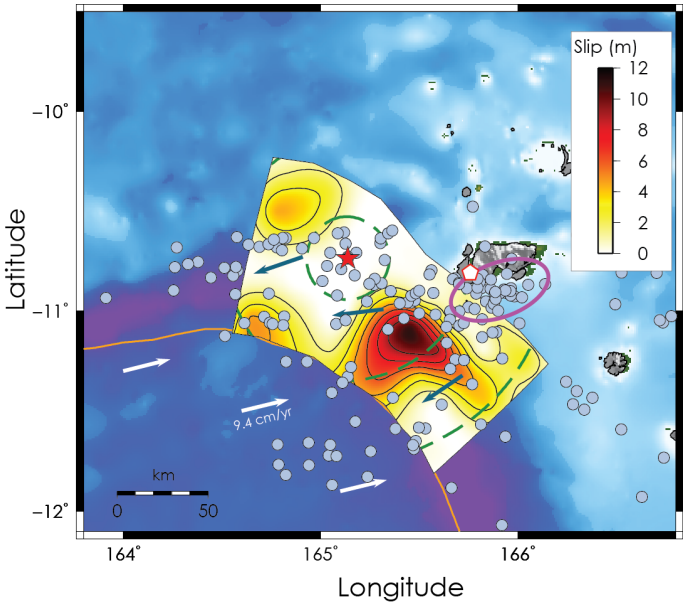


**Figure 4.** Coseismic tsunami source of the 2013 Santa Cruz Islands earthquake. Slip model is contoured (black solid line) in 1.5 m intervals. Blue arrows indicate the rake. White arrows indicate the convergence direction of the Australian Plate. Cyan dots represent the early aftershocks (occurred by 48 h after the mainshock, NEIC catalogue). Magenta ellipse approximately indicates the cluster of right-lateral strike-slip aftershock events. White pentagon indicates the area where have been observed the maximum tsunami wave heights (Fritz et al., 2014; NOAA/NGDC, http://www.ngdc.noaa.gov/hazard/tsu_db.shtml). Green dashed circles represent the rupture front expansion (rupture velocity 1.5 km $s^{-1}$) at 15, 45, and 75 s.





NHESSD
3, 1949–1970, 2015



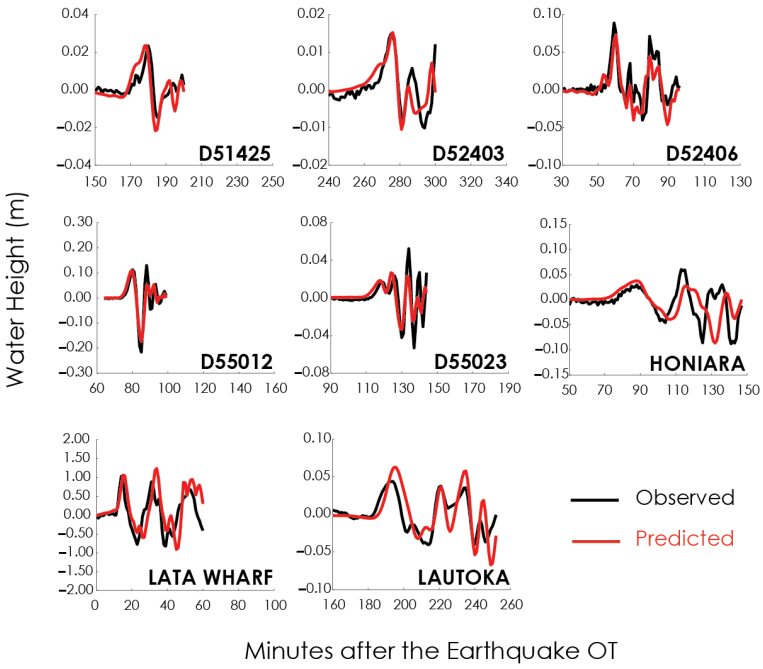


**Figure 5.** Data fit. Comparison between observed (black) and predicted (red) tsunami data.





NHESSD
3, 1949–1970, 2015



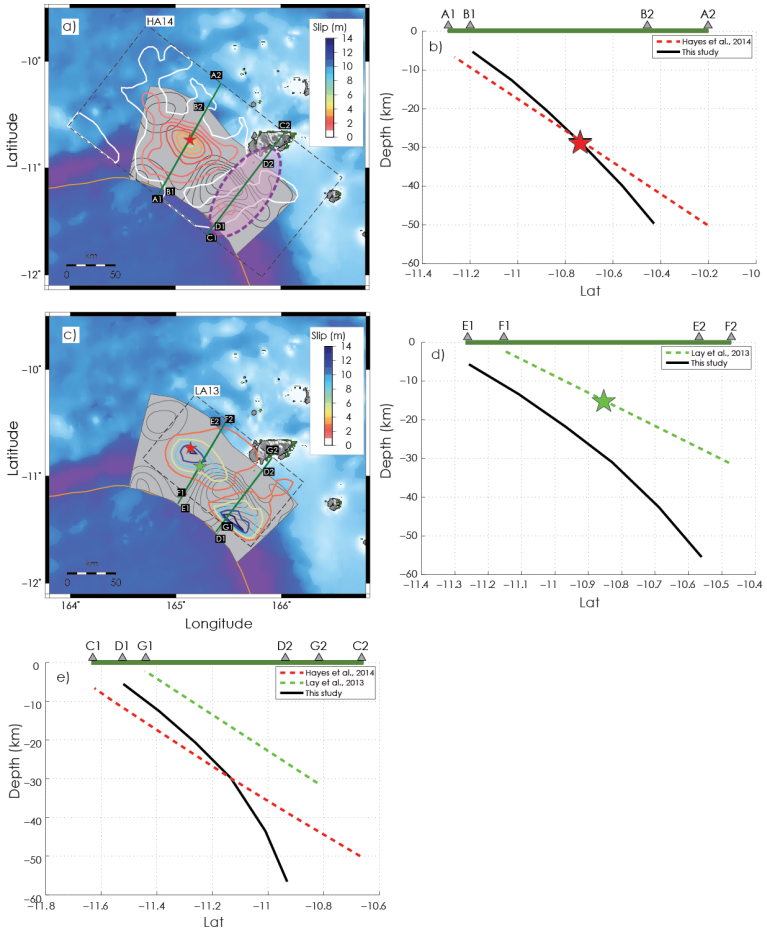






NHESSD

3, 1949–1970, 2015

# 6 February 2013 $M_w$ 8.0 Santa Cruz Islands Tsunami

F. Romano et al.



**Figure 6.** Comparison with other source models. **(a)** HA14 model (coloured solid lines at 0.5 m intervals); magenta ellipse approximately represents the aseismic slip area hypothesized in HA14; black solid lines as in Fig. 4; green solid lines represent the surface projections of the depth profiles along the HA14 fault model and that one adopted in this study. **(b)** Depth profiles along the HA14 fault model (red) and that one adopted in this study (black) crossing the hypocenter used in HA14 (red star) and in this study (black star); notice that the two hypocenters are almost coincident. **(c)** LA13 model (coloured solid lines at 2.8 m intervals); black solid lines as in Fig. 4; green solid lines represent the surface projections of the depth profiles along the LA13 fault model and that one adopted in this study. **(d)** Depth profiles along the LA13 fault model (green) and that one adopted in this study (black) crossing the hypocenter used in LA13 (green star) and in this study (black star). **(e)** Depth profiles along the LA13 and HA14 fault models and that one adopted in this study crossing the aseismic slip area hypothesized in HA14.





NHESSD
3, 1949–1970, 2015